Dalton Transactions

ROYAL SOCIETY OF CHEMISTRY

PAPER

View Article Online
View Journal | View Issue



Cite this: *Dalton Trans.*, 2025, **54**, 11006

# Solvent-free mechanochemical access to phase-pure Cs–Co–Cl halometalates with tuneable electronic properties for energy applications†

Pablo Garrido,[a] Darío Espinoza,[a] Karem Gallardo,[b] Rosa M. González-Gil[c] and Rodrigo Castillo *[d]

We report a solvent-free mechanochemical route for the selectively synthesis of three different caesium cobalt chlorides: $CsCoCl_3$, $Cs_2CoCl_4$, and $Cs_3CoCl_5$, by simply tuning the $CsCl : CoCl_2$ precursor ratio. This is the first comprehensive comparative study of these phases synthesized in pure form, enabling a clear correlation between composition, crystal structure, and optoelectronic properties. Each phase exhibits a unique $Co^{2+}$ coordination geometry: octahedral in $CsCoCl_3$ and tetrahedral in $Cs_2CoCl_4$ and $Cs_3CoCl_5$, as revealed by XRD, SEM-EDS, Raman, and XPS, with several features reported here for the first time. All phases display high thermal stability and narrow optical bandgaps (1.65–1.70 eV), supported by ligand field analysis and CIE colorimetry. Valence and conduction band energies determined by VB-XPS and cyclic voltammetry reveal a systematic, composition-driven tuning of energy levels across the series. Importantly, the band edge alignment are suitable for visible-light-driven hydrogen evolution and photovoltaic applications. SCAPS-1D simulations predict power conversion efficiencies up to 17.1%, positioning these halocobaltates as promising absorbers. Altogether, this work introduces a scalable synthesis route and demonstrates the potential of cobalt-based halide frameworks as modular systems for solar energy conversion and photocatalysis.

Received 10th June 2025,
Accepted 24th June 2025

DOI: 10.1039/d5dt01355k

rsc.li/dalton



## Introduction

There has been a renewed and growing interest in metal halide perovskites, both hybrid and fully inorganic, driven by their remarkable optoelectronic properties and wide range of potential applications. This resurgence was undoubtedly triggered by the success of the hybrid perovskite $CH_3NH_3PbI_3$,[1,2] whose outstanding semiconducting behavior and light-harvesting capability in solar cells have led to an unprecedented increase in power conversion efficiencies, reaching over 30% within a decade.[3,4] This breakthrough not only underscored the potential of metal halide frameworks for photovoltaics, but also catalyzed intensive research into lead-free alternatives with improved stability and compositional flexibility.[5–13] In particular, the pursuit of non-toxic, thermally stable, and compositionally tunable alternatives has turned attention to new families of halide perovskites and perovskitoids, aiming to preserve the desirable optical and structural features while expanding chemical diversity.[14–16]

This exploration has naturally extended to transition metal-based halide systems, where replacing lead with other metals introduces opportunities to modulate structural, magnetic, and optical properties.[17–26] Cobalt-based halides are especially intriguing due to the flexible coordination chemistry of $Co^{2+}$, and its characteristic d–d electronic transition within the visible and near-infrared range. These features make cobalt halides attractive candidates for light-absorbing and photoactive materials, with potential applications beyond conventional photovoltaics. Within this family, the $CsCl–CoCl_2$ system contains three well-defined stoichiometric phases: $CsCoCl_3$, $Cs_2CoCl_4$, and $Cs_3CoCl_5$, each featuring distinct structural motifs and cobalt coordination environments. However, despite their compositional simplicity and structural richness, these compounds have remained synthetically challenging to isolate as pure phases *via* conventional methods, and as a result, there is a limited body of work reporting their

[a]*Departamento de Química, Universidad Católica del Norte, Antofagasta, Chile*
[b]*Instituto de Ciencias Aplicadas, Facultad de Ingeniería, Universidad Autónoma de Chile, San Miguel, Santiago, Chile*
[c]*Novel Energy-Oriented Materials Group at Catalan Institute of Nanoscience and Nanotechnology (ICN2) CSIC and BIST, Campus UAB, Barcelona, Spain*
[d]*Facultad de Química y de Farmacia, Pontificia Universidad Católica de Chile, Macul, Santiago, Chile. E-mail: rodrigo.castillo@uc.cl*

†Electronic supplementary information (ESI) available: SEM-EDS, crystallographic tables. See DOI: https://doi.org/10.1039/d5dt01355k

properties, and many of their fundamental characteristics as well as potential applications, remain poorly understood. Among the well-established characteristics of these phases is their magnetic behavior. $CsCoCl_3$ exhibits Ising-like antiferromagnetic ordering with frustrated interchain interactions at low temperatures.[27,28] $Cs_2CoCl_4$ behaves as a quasi-one-dimensional antiferromagnet with $Co^{2+}$ ($S = \frac{1}{2}$) chains and XY-type interactions, showing long-range order below 22 K.[29,30] $Cs_3CoCl_5$ displays magnetic anisotropic due to spin–orbit coupling and crystal field effects, and can be described by an effective $S = 1$ spin Hamiltonian.[31]

The crystallization behavior of $CsCoCl_3$, $Cs_2CoCl_4$, and $Cs_3CoCl_5$ has been studied using both melt- and solution-based approaches, revealing significant differences in phase stability, compositional constraints, and synthesis times. Among the three, $Cs_2CoCl_4$ is the most synthetically accessible, readily forming from stoichiometric mixtures *via* slow evaporation over several days.[32,33] $CsCoCl_3$, by contrast, has only been obtained from melts using a slight excess of $CoCl_2$,[34,35] or from aqueous solution under narrowly controlled evaporation conditions and with a large excess of $CoCl_2$.[36] $Cs_3CoCl_5$ requires an excess of CsCl and similarly tight compositional windows, whether synthesized from melt or in solution, typically over long evaporation periods.[32,37–39]

In this context, mechanochemical synthesis has emerged as a powerful alternative for the preparation of inorganic compounds, particularly in systems where conventional methods are limited by solubility, volatility, or selectivity.[40,41] This solvent-free approach enables the direct formation of crystalline materials under ambient conditions, often with superior control of stoichiometry and without requiring prolonged thermal treatments.[42] Notably, mechanochemistry has proven especially effective for accessing metastable phases, complex halide and oxyhalide systems, and compounds that are otherwise inaccessible or unstable in melt or solution routes.[43–47]

In the present work, we report the solvent-free mechanochemical synthesis of the halocobaltate phases $CsCoCl_3$, $Cs_2CoCl_4$, and $Cs_3CoCl_5$, as phase-pure products obtained by direct reaction of stoichiometric amounts of CsCl and $CoCl_2$ under ambient conditions. A comprehensive characterization of the materials is presented, including structural analysis by powder X-ray diffraction (XRD), morphological inspection by scanning electron microscopy (SEM), and vibrational analysis through Raman spectroscopy. The thermal behavior was assessed using simultaneous thermogravimetric analysis and differential scanning calorimetry (TGA-DSC). Furthermore, optical absorption was investigated *via* UV-Vis-NIR spectroscopy and diffuse reflectance, and the electronic structure of each compound was probed using valence-band XPS, cyclic voltammetry (CV), and solar cell simulations performed with the SCAPS-1D software. These results not only demonstrate the efficacy of mechanochemistry for accessing halide phases with controlled stoichiometry but also provide new insights into the structure–property relationships and highlight their potential in optoelectronic and photovoltaic applications.

# Experimental

## Materials and synthesis

All sample handling was performed under an Ar atmosphere. Caesium chloride (CsCl, ≥98%, Sigma-Aldrich) and cobalt(II) chloride ($CoCl_2$, 97%, Sigma–Aldrich) were weighed in molar ratios of 1 : 1, 2 : 1, and 3 : 1, to synthesize $CsCoCl_3$, $Cs_2CoCl_4$, and $Cs_3CoCl_5$, respectively. The mixtures were loaded into 50 mL stainless steel jars along with 8 mm stainless steel balls, maintaining a ball-to-sample mass ratio of 100 : 1. The jars were mounted in a TMAX-XQM planetary ball mill and operated at 500 rpm for 60 minutes.

## Characterization

**X-ray powder diffraction (XRD)** was carried out using a Malvern PANalytical diffractometer equipped with Cu Kα radiation ($\lambda$ = 1.54056 Å) and a linear X'Celerator detector, covering the angular range $5° < 2\theta < 70°$. Full-profile refinements were performed by the Rietveld method as implemented in the Jana2020 software.[48]

**Scanning electron microscopy (SEM)** images were acquired on a FEI Quanta 650 FEG, operated at 30 kV in high-vacuum mode. Elemental analysis was carried out using an Inca 250 SSD XMax20 detector. Quantification was performed using ZAF correction procedures and calibrated against appropriated standards: KCl for Cl, and Co metal for Co.

**X-ray photoelectron spectroscopy (XPS)** measurements were performed using a STAIB Instrument Surface Analysis Station 1 RQ300/2, with Al Kα radiation ($\lambda$ = 1486.6 eV) as the excitation source.

**Raman spectroscopy** was conducted using a Jasco NRS-4500 confocal Raman microscope, equipped with a Peltier-cooled CCD detector and a 532 nm laser. Spectra were collected over the 50–3600 $cm^{-1}$ range with a 2 $cm^{-1}$. Each spectrum was acquired by accumulating six 50 seconds scans at a laser power of 1.8 mW with 10% attenuation to minimize sample degradation.

**Thermal analysis** was carried out using a Netzsch Jupiter STA 449 instrument for simultaneous thermogravimetric analysis (TGA) and differential scanning calorimetry (DSC). Heating and cooling rates were 10 °C $min^{-1}$ under nitrogen flow (50 mL $min^{-1}$), in the temperature range of 20 °C–700 °C.

**UV-Vis-NIR spectroscopy** was performed using a Jasco V-770 spectrophotometer equipped with an integrating sphere to account for diffuse reflectance. Spectra were collected from 200 to 2500 nm on polycrystalline powders at room temperature, using $BaSO_4$ as a non-absorbing reference. The reflectance data were converted using the Kubelka–Munk transformation, $F(R) = ((1 - R)^2/2R)$, and optical bandgaps were estimated by extrapolating the linear region of the Tauc plots. Additionally, CIE Lab* color coordinates were extracted from the reflectance spectra using the Color Analysis module in JASCO Spectra Manager (D65 standard illuminant, 10° observer, 380–780 nm), providing quantitative assessment of the perceived sample color.

**Electrochemical measurements** were performed on a BioLogic VMP3 potentiostat using a conventional three-electrode configuration. The working electrode consisted of a glassy carbon disk (0.0707 $cm^2$) modified with a drop-cast ink prepared by dispersing 10 mg of the sample in 1 mL of methanol and 10 μL of Nafion. A platinum wire and silver wire were used as the counter and reference electrodes, respectively, the latter connected *via* a salt bridge containing 0.1 M tetraethylammonium tetrafluoroborate ($TEABF_4$, 99%, Acros Organics) in dichloromethane ($CH_2Cl_2$, ≥99.5%, Sigma–Aldrich). Measurements were carried out in an inert atmosphere using the same electrolyte. A ferrocene/ferrocenium ($Fc/Fc^+$) redox couple (50 mM ferrocene, Sigma–Aldrich) dissolved in 0.1 M $TEABF_4/CH_2Cl_2$ was employed as an internal pseudoreference for potential calibration. The onset of oxidation and reduction processes were used to estimate the valence and conduction band edge positions.

**Solar cell simulations** were performed using SCAPS-1D (version 3.3.12, University of Ghent).[49,50] A planar n-i-p device structure was modeled with the architecture FTO/$TiO_2$/absorber/Spiro-OMeTAD, employing layer thicknesses of 100, 30, 200, and 90 nm, respectively. Standard parameters for FTO, $TiO_2$, and Spiro-OMeTAD were taken from literature and SCAPS databases,[51] while absorber parameters such as bandgap, electron affinity and energy levels were experimentally derived. The absorbers were modeled as lightly n-doped semiconductors (donor concentration $1 \times 10^{15}$ $cm^{-3}$), with carrier mobilities set to 5 $cm^2$ $V^{-1}$ $s^{-1}$, effective density of states ($N_c$ and $N_v$) of $2 \times 10^{18}$ $cm^{-3}$, and a dielectric constant of 9.0. A mid-gap trap with a density of $1 \times 10^{15}$ $cm^{-3}$ was also included. Simulations were conducted under AM1.5G illumination (100 mW $cm^{-2}$, 300 K), yielding key photovoltaic parameters such as *J–V* curves, short-circuit current ($J_{sc}$), open-circuit voltage ($V_{oc}$), fill factor (FF), and power conversion efficiency (PCE).

## Results and discussion

The three caesium cobalt chloride phases synthesized *via* direct mechanochemical milling are readily distinguishable by their characteristic colours, which reflect differences in cobalt coordination geometry. $CsCoCl_3$ exhibits a turquoise hue, consistent with high-spin $Co^{2+}$ in octahedral environment, while $Cs_2CoCl_4$ and $Cs_3CoCl_5$ appear cyan-blue, indicating tetrahedral coordination. All samples are highly sensitive to moisture and air, gradually turning purple upon exposure due to hydration and the formation of $Co^{2+}$-aquo species. The structural identity and crystallinity of the mechanosynthesized products were confirmed by powder X-ray diffraction and Rietveld refinements (Fig. 1 top). The experimental patterns match closely the calculated models, and the low residuals support the phase purity and structural fidelity of the synthesized materials (Table S1†). $CsCoCl_3$ and $Cs_2CoCl_4$ were refined as single-phase products, whereas the $Cs_3CoCl_5$ sample displays a minor impurity attributed to CsCl, evidenced by a weak reflection near $2\theta \approx 21.6°$. The slightly elevated background observed in all patterns is attributed to diffuse scattering from adsorbed moisture, a common feature in air-sensitive chlorides. These results demonstrate the successful and selective formation of each target phase under solvent-free conditions. Structurally, the three compounds exhibit distinct $Co^{2+}$ coordi-

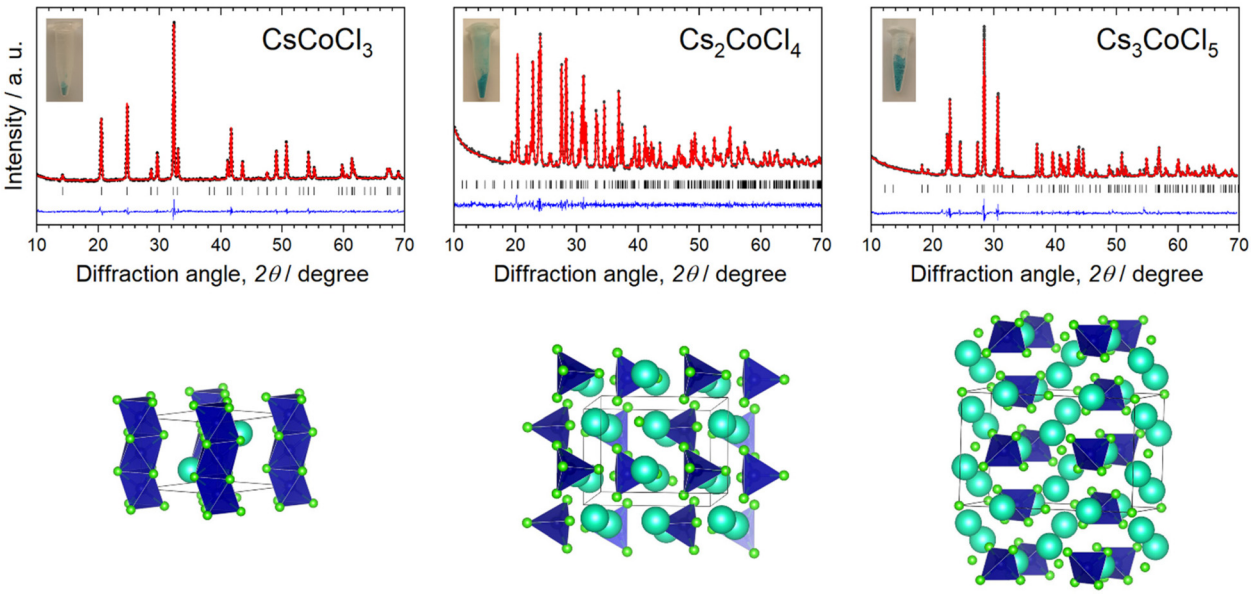


**Fig. 1** (Top) Rietveld-refined X-ray diffraction patterns (black points: observed; red line: calculated; blue line: difference; black ticks: reflections position) of mechanochemically synthesized samples. Inset show the visual appearance of each sample. (bottom) Crystal structures illustrating the progression from infinite columns of face-sharing $CoCl_6$ octahedra to isolated tetrahedra. Green, purple-blue, and cyan spheres represent Cl, Co, and Cs atoms, respectively.

nation environments that evolve with increasing Cs : Co ratio. $CsCoCl_3$ crystallizes in a hexagonal structure featuring infinite columns of face-sharing $CoCl_6$ octahedra aligned along the [001] axis. In contrast, $Cs_2CoCl_4$ adopts an orthorhombic structure with isolated $CoCl_4$ tetrahedra distributed throughout the lattice. $Cs_3CoCl_5$ also contains discrete $CoCl_4$ tetrahedra embedded in a three-dimensional array where $Cs^+$ cations bridge and stabilize isolated $CoCl_4^{2-}$ tetrahedra. The refined crystallographic parameters for each phase are summarized in Table S1.†

The morphology and elemental homogeneity of the $CsCoCl_3$, $Cs_2CoCl_4$, and $Cs_3CoCl_5$ samples were examined by SEM and EDS. As shown in Fig. S1,† all three phases exhibit compact polycrystalline aggregates, with particle sizes in the range of 1–10 μm. $CsCoCl_3$ displays larger faceted domains with angular edges, while $Cs_2CoCl_4$ and $Cs_3CoCl_5$ reveal more granular morphologies composed of rounded, densely packed particles. Elemental mapping (Fig. S2–S4†) confirms that Cs, Co, and Cl are homogeneously distributed throughout the selected crystallites for all three compositions. Quantitative EDS analysis, calibrated using external standards, further supports the expected stoichiometries, with atomic ratios in excellent agreement with the nominal Cs : Co : Cl values of 1 : 1 : 3, 2 : 1 : 4, and 3 : 1 : 5, respectively. These results validate the compositional uniformity and phase purity of the mechanochemically synthesized samples.

X-ray photoelectron spectroscopy was used to assess the oxidation state and local chemical environment of cobalt in the three synthesized samples (Fig. 2a). The Co 2p core-level spectra of all three samples display two principal peaks corresponding to Co $2p_{3/2}$ and Co $2p_{1/2}$ centered at ~781 and ~796 eV, respectively. The observed spin–orbit splitting (15.44–15.91 eV) and the presence of characteristics shake-up satellites confirm the $Co^{2+}$ state.[52] Although the binding energies differ only slightly among the samples, notable variations are observed in the full width at half maximum (FWHM) of the $2p_{3/2}$ peak: $CsCoCl_3$ exhibits the narrowest signal (3.28 eV), followed by $Cs_3CoCl_5$ (3.31 eV) and $Cs_2CoCl_4$ (3.591 eV). These differences likely reflect variations in local symmetry and electronic delocalization, with the sharper signal in $CsCoCl_3$ indicative of greater structural order, consistent with its octahedral coordination of $Co^{2+}$, while broader peaks in $Cs_2CoCl_4$ and $Cs_3CoCl_5$ align with more distorted tetrahedral environments.[53–55] These results corroborate the phase-dependent structural motifs and confirm the uniform +2 oxidation state of cobalt across the series.

The low-frequency Raman spectra (< 400 $cm^{-1}$) of the samples reveal distinct vibrational signatures consistent with their respective cobalt coordination environments and crystallographic symmetries (Fig. 2b). In $CsCoCl_3$, the spectrum resolves five well-defined modes corresponding to the expected $A_{1g} + E_{1g} + 3E_{2g}$ representations of the $P6_3/mmc$ space group.[56,57] For the orthorhombic lattice of $Cs_2CoCl_4$, the spectrum exhibits broad overlapping bands characteristics of its rich vibrational manifold (42 Raman-active modes). Three regions can be discerned: lattice modes (< 100 $cm^{-1}$), Cl–Co–Cl bending modes (100–140 $cm^{-1}$), and Co–Cl stretching modes (> 280 $cm^{-1}$).[58,59] $Cs_3CoCl_5$ also shows distinct tetra-

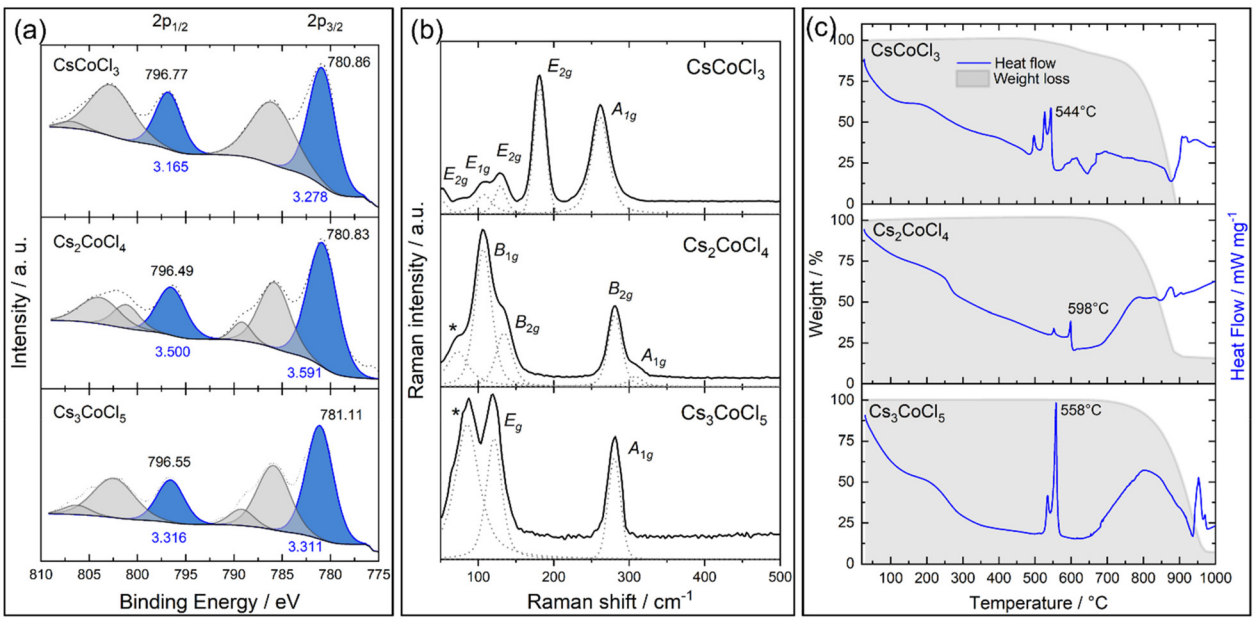


**Fig. 2** (a) High-resolution Co 2p XPS spectra of $CsCoCl_3$, $Cs_2CoCl_4$, and $Cs_3CoCl_5$, showing characteristic $Co^{2+}$ $2p_{3/2}$ and $2p_{1/2}$ peak and satellite features; full width at half maximum (FWHM, in eV) values are indicated. (b) Raman spectra of the three phases, highlighting vibrational fingerprints corresponding to octahedral and tetrahedral Co–Cl coordination environments, as well as lattice modes indicated by *. (c) Thermogravimetric and differential scanning calorimetry (TGA-DSC) profiles showing thermal stability and endothermic transitions up to the melting points of each compound.

hedral $CoCl_4$ vibrational signatures with three main bands at 87, 120, and 282 $cm^{-1}$, assigned respectively to external lattice, bending ($E_g$), and symmetric stretching ($A_{1g}$) modes. These assignments are in good agreement with reports on structurally analogous $Cs_3MCl_5$ compounds (M = Fe, Cd, Mg).[60–62]

The thermal behaviour evaluated by TGA-DSC shows different features for each phase (Fig. 2b). $CsCoCl_3$ displays three endothermic transitions, with the most intense event at 544 °C attributed to congruent melting. Lower-temperature peaks at 497 °C and 527 °C are assigned to eutectic equilibria involving $Cs_2CoCl_4$ and $CoCl_2$. $Cs_2CoCl_4$ shows thermal events at 522 °C and 598 °C, the latter corresponding to its congruent melting. $Cs_3CoCl_5$ exhibits transitions at 534 °C and 558 °C, also consistent with eutectic and melting processes.[63] These results confirm the thermal stability of all three compounds well above room temperature and establish their feasibility for integration into functional devices processed at moderated to high temperatures.

Optical absorption measurements reveal distinct spectral signatures consistent with the $Co^{2+}$ coordination environment in each phase (Fig. 3a). $CsCoCl_3$ exhibits three well-defined spin-allowed transitions at approximately 1646, 826, and 600 nm, corresponding to the $^4T_1(F) \rightarrow {}^4T_2(F)$, $^4A_2(F)$, and $^4T_1(P)$ excitations, respectively.[64] On the other hand, $Cs_2CoCl_4$ and $Cs_3CoCl_5$ show nearly identical spectra characterized by two spin-allowed transitions at 1942 and 670 nm, assigned to the $^4A_2(F) \rightarrow {}^4T_1(F)$ and $^4T_1(P)$ transitions. Analysis of these transitions using Tanabe–Sugano diagrams allowed the extraction of ligand field parameters (Table S2†), which corroborate the structural assignments: octahedral $Co^{2+}$ in $CsCoCl_3$ exhibits a larger ligand field splitting ($\Delta$), while the slightly lower Racah ($B$) and nephelauxetic ($\beta$) parameters observed in the tetrahedral $Co^{2+}$ phases suggest more localized and covalent Co–Cl interactions in $Cs_2CoCl_4$ and $Cs_2CoCl_5$. Additionally, colorimetric analysis based on the measured spectra further supports these distinctions, yielding CIE Lab coordinates (Table S1†) that differentiate the samples by hue: turquoise for $CsCoCl_3$ and cyan-blue for $Cs_2CoCl_4$ and $Cs_3CoCl_5$ (Fig. 3a, inset).

Building on these ligand field characteristics, the optical bandgaps energies were evaluated by diffuse reflectance spectroscopy using the Kubelka–Munk transformation (Fig. 3b). All three compounds exhibit absorption edges in the near infrared to visible region, confirming their nature as narrow bandgap semiconductors. For $Cs_2CoCl_4$ and $Cs_3CoCl_5$, a sharp absorption was observed at 1.66 and 1.65 eV, respectively. In contrast, $CsCoCl_3$ displays a more complex spectrum consisting of two main features: a subtle absorption at 1.50 eV associated with

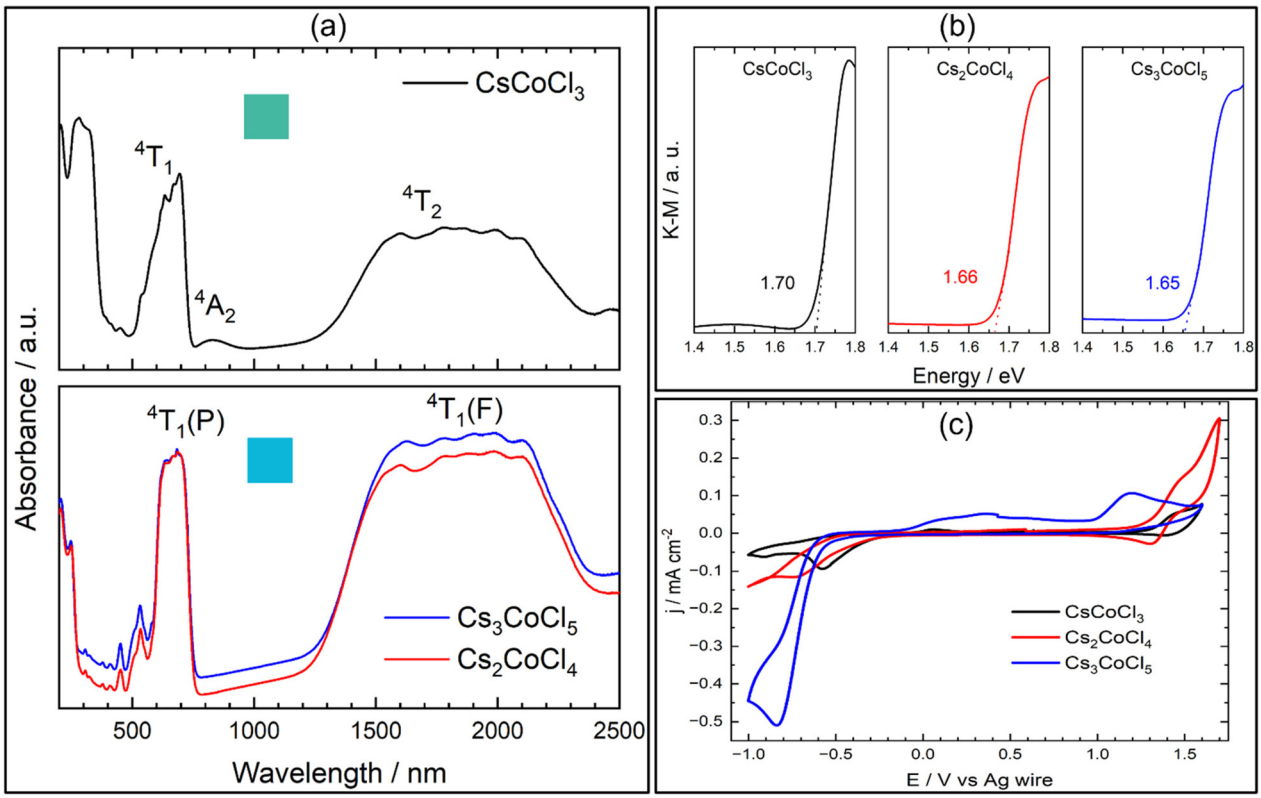


**Fig. 3** (a) Optical absorption spectra showing $Co^{2+}$ d-d transitions in $CsCoCl_3$ (octahedral) and $Cs_2CoCl_4$/$Cs_3CoCl_5$ (tetrahedral). Forbidden transitions are not indicated. (b) Tauc plots derived from diffuse reflectance (Kubelka–Munk function), used to estimate the optical bandgaps: 1.70 eV ($CsCoCl_3$), 1.66 eV ($Cs_2CoCl_4$), and 1.65 eV ($Cs_3CoCl_5$). (c) Cyclic voltammetry profiles used to extract onset oxidation and reduction potentials for estimation of valence and conduction band positions.

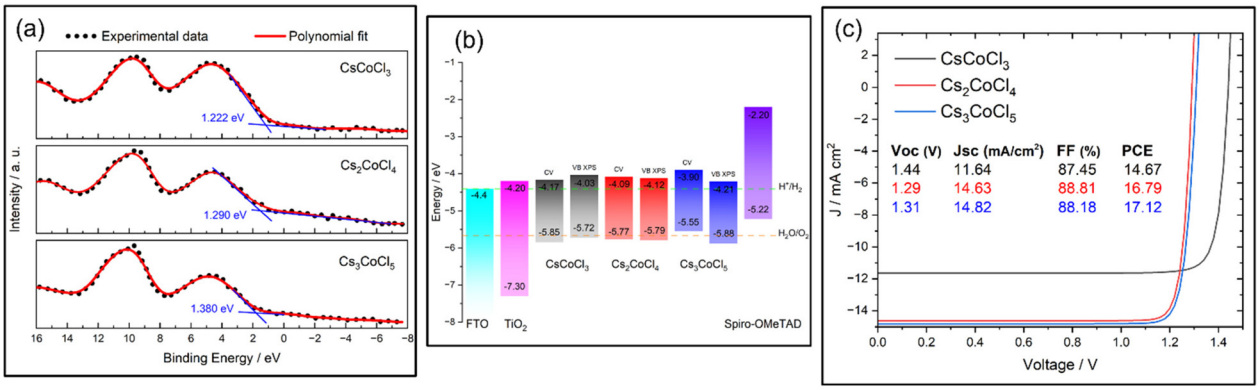


**Fig. 4** (a) Valence band spectra obtained by XPS, showing extrapolated onsets used to determine EVB values. (b) Absolute energy level diagrams of $CsCoCl_3$, $Cs_2CoCl_4$, and $Cs_3CoCl_5$ determined by CV and VB-XPS, compared with common charge transport layers (FTO, $TiO_2$, Spiro-OMeTAD) and redox potentials of water ($H^+/H_2$ and $H_2O/O_2$). (c) Simulated *J*–*V* curves for planar heterojunction solar cells using each compound as the absorber layer (FTO/$TiO_2$/absorber/Spiro-OMeTAD), highlighting the predicted performance metrics: open-circuit voltage ($V_{oc}$), short-circuit current ($J_{sc}$), fill factor (FF), and power conversion efficiency (PCE).

internal d-d transition, and a stronger onset around 1.70 eV attributed to the optical bandgap. These results reinforce the electronic distinctions between octahedral and tetrahedral $Co^{2+}$ environments and support the potential of these compounds for low-bandgap optoelectronic applications.

To further explore the electronic properties, cyclic voltammetry was employed to estimate the frontier energy levels of the three compounds (Fig. 3c).[65] The valence band (EVB) and conduction band (ECB) energies were calculated from the oxidation and reduction onset potentials, using the ferrocene/ferrocenium ($Fc/Fc^+$) couple as an internal reference (−4.80 eV *vs.* vacuum, Fig. S5†).[66–68] For $CsCoCl_3$, EVB and ECB were determined to be −5.85 eV and −4.17 eV, respectively, yielding an electrochemical bandgap of 1.68 eV. Similarly, $Cs_2CoCl_4$ and $Cs_3CoCl_5$ exhibit EVB/ECB values of −5.78/−4.11 eV and −5.55/−3.90 eV, respectively, with corresponding bandgaps of 1.67 and 1.65 eV. These values are in excellent agreement with the optical bandgaps derived from diffuse reflectance, confirming the reliability of the methods and reinforcing the intrinsic semiconducting character of the phases.

To corroborate the electrochemical data and further probe the electronic structure, valence band XPS was performed. The EVB values were extracted from the extrapolated leading edges of the spectral and referenced to the vacuum level (Fig. 4a). For $CsCoCl_3$, $Cs_2CoCl_4$, and $Cs_3CoCl_5$, the EVB positions were determined to be −5.72, −5.79, and −5.88, respectively. By subtracting the optical bandgaps determined from diffuse reflectance spectroscopy, the corresponding ECB were estimated as −4.03, −4.12, and −4.21 eV. These values are consistent with those obtained by CV, validating the internal consistency between spectroscopic and electrochemical methods. The progressive downshift of both EVB and ECB across the $CsCoCl_3$–$Cs_2CoCl_4$–$Cs_3CoCl_5$ series (Fig. 4b) reflects the effect of compositional variation on band edges positions. Altogether, these findings confirm the narrow bandgap semiconducting nature of these materials and reveal the potential for fine-tuning their electronic structure through structural and chemical modification.

The absolute energy level diagrams derived from VB XPS, CV, and optical spectroscopy suggest that $CsCoCl_3$, $Cs_2CoCl_4$, and $Cs_3CoCl_5$, are promising candidates for optoelectronic and photocatalytic applications. All three compounds exhibit conduction band minima above the $H^+/H_2$ reduction potential (−4.44 eV) and valence band maxima below the $H_2O/O_2$ oxidation potential (−5.67 eV), indicating their thermodynamic suitability for overall water splitting under visible light irradiation (Fig. 4b).[69,70] Additionally, their band edge alignment is compatible with common charge transport materials used in photovoltaic devices: electron extraction by $TiO_2$ (ECB = −4.0 eV) or $SnO_2$ (ECB = −4.2 eV), and hole extraction by $NiO_x$ (EVB = −5.4 eV) or Spiro-OMeTAD (EVB = −5.2 eV) would be energetically favorable.[71–73]

Given this energetic compatibility, the photovoltaic potential of these materials was further evaluated through SCAPS-1D simulations. Planar heterojunction solar cells with a standard FTO/$TiO_2$/absorber/Spiro-OMeTAD architecture were modeled for each compound. The predicted power conversion efficiencies (PCE) reached 14.7% for $CsCoCl_3$, 16.8% for $Cs_2CoCl_4$, and 17.1% for $Cs_3CoCl_5$, driven by high open-circuit voltages and fill factors above 87% (Fig. 4c). The higher PCEs of the tetrahedral phases reflect their narrower bandgaps and improved alignment within the devices stack. While these simulations represent idealized conditions, they underscore the potential of Cs–Co–Cl halometalates as compositionally tunable absorbers for low-bandgap photovoltaics and integrated solar-driven systems.

## Conclusions

In this work, we have conducted the first comprehensive comparative study of the cobalt chloride phases $CsCoCl_3$,

$Cs_2CoCl_4$, and $Cs_3CoCl_5$, synthesized as phase-pure materials *via* a rapid and solvent-free mechanochemical approach. By tuning the $CsCl:CoCl_2$ ratio, each phase was selectively obtained within one hour, highlighting the efficiency and precision of this method. Detailed structural, spectroscopic, and electronic characterizations, including SEM-EDS mapping, CV, and VB XPS, are presented here for the first time for this family of halide cobaltates. The compounds feature distinct structural motifs, octahedral $Co^{2+}$ in $CsCoCl_3$ and tetrahedral $Co^{2+}$ in $Cs_2CoCl_4$ and $Cs_3CoCl_5$, which result in well-defined differences in their vibrational, optical, and electronic properties. This clear structure–property correlation is evidenced by their unique Raman fingerprints, d–d transitions, ligand field parameters, and colorimetric profiles. Bandgaps in the narrow 1.65–1.70 eV range were confirmed by both optical and electrochemical methods, and absolute band edge positions obtained by VB XPS reveal systematic shifts in EVB and ECB with increasing Cs content, highlighting the tunability of their electronic structure *via* coordination and compositional control. Thermal analysis confirms the robustness of all three phases up to their melting points, and their band alignments are well-positioned for both photocatalytic water splitting and photovoltaic applications. SCAPS-1D simulations further support this, predicting PCEs exceeding 17% under ideal conditions, placing these materials among promising candidates for low bandgap solar absorbers.

Overall, this study introduces an efficient synthetic strategy and reveals key structure–property relationships, establishing cobalt-based halide frameworks as a versatile platform for future optoelectronic and solar energy technologies.

## Author contributions

Rodrigo Castillo contributed to supervision, project administration, and writing – review & editing. Pablo Garrido was responsible for investigation, methodology, and writing – original draft. Darío Espinoza contributed to supervision, data curation, and validation. Karem Gallardo was involved in funding acquisition, provision of resources, and validation. Rosa M. González-Gil contributed to data curation, formal analysis, and provision of resources.

## Conflicts of interest

There are no conflicts to declare.

## Data availability

Necessary datasets supporting this article have been included in the ESI.† Additional raw data, including crystallographic information files (CIFs), Rietveld refinement input/output files, and spectroscopic data, are available from the corresponding author upon reasonable request.

## Acknowledgements

R. C. thanks to Fondecyt Iniciación (11230732). P. G. thanks to Beca UCN and ICN2. K. G. thanks to Fondecyt Iniciación (11230831). Authors thank to Unidad de Equipamiento Científico MAINI-UCN, and to FONDEQUIP EQM 210078. Authors acknowledge Prof. Pedro Gómez for valuable discussion.

## References

1 C. C. Stoumpos and M. G. Kanatzidis, The renaissance of halide perovskites and their evolution as emerging semiconductors, *Acc. Chem. Res.*, 2015, **48**, 2791–2802.
2 L. Mao, J. Chen, P. Vishnoi and A. K. Cheetham, The renaissance of functional hybrid transition-metal halides, *Acc. Mater. Res.*, 2022, **3**, 439–448.
3 S. Kim, T. T. Trinh, J. Park, D. P. Pham, S. Lee, H. B. Do, N. N. Dang, V. A. Dao, J. Kim and J. Yi, Over 30% efficiency bifacial 4-terminal perovskite-heterojunction silicon tandem solar cells with spectral albedo, *Sci. Rep.*, 2021, **11**, 15524.
4 A. Harter, K. Artuk, F. Mathies, O. Karalis, H. Hempel, A. Al-Ashouri, S. Albrecht, R. Schlatmann, C. Ballif, B. Stannowski and C. M. Wolff, Perovskite/silicon tandem solar cells above 30% conversion efficiency on submicron-sized textured Czochralski-silicon bottom cells with improved hole-transport layers, *ACS Appl. Mater. Interfaces*, 2024, **16**, 62817–62826.
5 R. L. Z. Hoye, R. E. Brandt, A. Osherov, V. Stevanovic, S. D. Stranks, M. W. B. Wilson, H. Kim, A. J. Akey, J. D. Perkins, R. C. Kurchin, J. R. Poindexter, E. N. Wang, M. G. Bawendi, V. Bulovic and T. Buonassisi, Methylammonium bismuth iodide as a lead-free, stable hybrid organic-inorganic solar absorber, *Chem. – Eur. J.*, 2016, **22**, 2605–2610.
6 M. Lyu, J. H. Yun, M. Cai, Y. Jiao, P. V. Bernhardt, M. Zhang, Q. Wang, A. Du, H. Wang, G. Liu and L. Wang, Organic-inorganic bismuth(III)-based material: a lead-free, air stable and solution-processable light-absorber beyond organolead perovskites, *Nano Res.*, 2016, **9**, 692–702.
7 M. Wang, W. Wang, B. Ma, W. Shen, L. Liu, K. Cao, S. Chen and W. Huang, Lead-free perovskite materials for solar cells, *Nano-Micro Lett.*, 2021, **13**, 62.
8 N. K. Tailor, S. Kar, P. Mishra, A. These, C. Kupfer, H. Hu, M. Awais, M. Saidaminov, M. I. Dar, C. Brabec and S. Satapathi, Advances in lead-free perovskite single crystals: fundamentals and applications, *ACS Mater. Lett.*, 2021, **3**, 1025–1080.
9 X. Li, J. Wu, S. Wang and Y. Qi, Progress of all-inorganic cesium lead-free perovskite solar cells, *Chem. Lett.*, 2019, **48**, 989–1005.
10 G. Volonakis, M. R. Filip, A. A. Haghighirad, N. Sakai, B. Wenger, H. J. Snaith and F. Giustino, Lead-free halide

 

double perovskites via heterovalent substitution of noble metals, *J. Phys. Chem. Lett.*, 2016, **7**, 1254–1259.

11 N. K. Noel, S. D. Stranks, A. Abate, C. Wehrenfennig, S. Guarnera, A. A. Haghighirad, A. Sadhanala, G. E. Eperon, S. K. Pathak, M. B. Johnston, A. Petrozza, L. M. Herz and H. J. Snaith, Lead-free organic-inorganic tin halide perovskites for photovoltaic applications, *Energy Environ. Sci.*, 2014, **7**, 3061–3068.

12 R. Nie, A. Mehta, B. W. Park, H. W. Kwon, J. Im and S. I. Seok, Mixed sulfur and iodide-based lead-free perovskite solar cells, *J. Am. Chem. Soc.*, 2018, **140**, 872–875.

13 R. Nie, R. R. Sumukam, S. H. Reddy, M. Banavoth and S. I. Seok, Lead-free perovskite solar cells enabled by hetero-valent substitutes, *Energy Environ. Sci.*, 2020, **13**, 2363–2385.

14 X. Li, Y. He, M. Kepenekian, P. Guo, W. Ke, J. Even, C. Katan, C. C. Stoumpos, R. D. Schaller and M. G. Kanatzidis, Three-dimensional lead iodide perovskitoid hybrids with high X-ray photoresponse, *J. Am. Chem. Soc.*, 2020, **142**, 6625–6637.

15 Q. Sun, Y. Xu, H. Zhang, B. Xiao, X. Liu, J. Dong, Y. Cheng, B. Zhang, W. Jie and M. G. Kanatzidis, Optical and electronic anisotropies in perovskitoid crystals of $Cs_3Bi_2I_9$ studies of nuclear radiation detection, *J. Mater. Chem. A*, 2018, **6**, 23388–23395.

16 T. Kong, H. Xie, Y. Zhang, J. Song, Y. Li, E. L. Lim, A. Hagfeldt and D. Bi, Perovskitoid-templeted formation of a 1D@3D perovskite structure toward highly efficient and stable perovskite solar cells, *Adv. Energy Mater.*, 2021, **11**, 2101018.

17 H. Shankar, A. Jha and P. Kar, Water-assisted synthesis of lead-free Cu based fluorescent halide perovskite nanostructures, *Mater. Adv.*, 2022, **3**, 658–664.

18 J. Qu, S. Xu, H. Shao, P. Xia, C. Lu, C. Wang and D. Ban, Recent progress of copper halide perovskites: properties, synthesis and applications, *J. Mater. Chem. C*, 2023, **11**, 6260–6275.

19 N. Navarro, R. Nelson, K. Gallardo and R. Castillo, Exploring the influence of cation and halide substitution in the structure and optical properties of $CH_3NH_3NiCl_3$ perovskite, *Molecules*, 2024, **29**, 2141.

20 N. Navarro, C. Núñez, D. Espinoza, K. Gallardo, I. Brito and R. Castillo, Synthesis, characterization, and photoelectric and electrochemical behavior of $(CH_3NH_3)_2Zn_{1(-x}Co_xBr_4$ perovskites, *Inorg. Chem.*, 2023, **62**, 17046–17051.

21 H. Zhou, X. Cui, C. Yuan, J. Cui, S. Shi, G. He, Y. Wang, J. Wei, X. Pu, W. Li, D. Zhang, J. Wang, X. Ren, H. Ma, X. Shao, X. Wei, J. Zhao, X. Zhang and J. Yin, Band-gap tuning of organic-inorganic hybrid palladium perovskite materials for a near-infrared optoelectronics response, *ACS Omega*, 2018, **3**, 13960–13966.

22 X. Cheng, L. Jing, Y. Yuan, S. Du, Q. Yao, J. Zhang, J. Ding and T. Zhou, Centimeter-size square 2D layered Pb-free hybrid perovskite single crystal $(CH_3NH_3)_2MnCl_4$ for red photoluminescence, *CrystEngComm*, 2019, **21**, 4085–4091.

23 J. Yin, X. Liu, L. Fan, J. Wei, G. He, S. Shi, J. Guo, C. Yuan, N. Chai, C. Wang, J. Cui, X. Wang, H. Zhou and D. Tian, Synthesis, crystal structure, absorption properties, photoelectric behavior of organic-inorganic hybrid $(CH_3NH_3)_2CoCl_4$, *Appl. Organomet. Chem.*, 2019, **33**, e4795.

24 T. Lee, D. B. Straus, X. Xu, W. Xie and R. J. Cava, Tunable magnetic transition temperatures in organic-inorganic hybrid cobalt chloride hexagonal perovskites, *Chem. Mater.*, 2023, **35**, 1745–1751.

25 J. B. Abdallah, C. J. Gómez-García and H. Boughzala, Synthesis, crystal structure, optical, thermal and magnetic studies of a new organic-inorganic hybrid based on tetrachloroferrate(III), *J. Solid State Chem.*, 2021, **303**, 122504.

26 R. Babu, A. K. Vardhaman, V. M. Dhavale, L. Giribabu and S. P. Singh, $MA_2CoBr_4$: lead-free cobalt-based perovskite for electrochemical conversion of water to oxygen, *Chem. Commun.*, 2019, **55**, 6779–6782.

27 W. B. Yelon, D. E. Cox and M. Eibschütz, Magnetic orfering in $CsCoBr_3$, *Phys. Rev. B*, 1975, **12**, 5007–5015.

28 F. Matsubara, S. Inawashiro and H. Ohhara, On the Raman scattering in $CsCoCl_3$, $CsCoBr_3$ and $RbCoCl_3$, *J. Phys.: Condens. Matter*, 1991, **3**, 1815–1826.

29 O. Breunig, M. Garst, A. Rosch, E. Sela, B. Buldmann, P. Becker, L. Bohatý, R. Müller and T. Lorenz, Low-temperature ordered phases of the spin-1/2 XXZ chain system in $Cs_2CoCl_4$, *Phys. Rev. B:Condens. Matter Mater. Phys.*, 2015, **91**, 024423.

30 K. Hirakawa, H. Yoshizawa, G. Shirane and H. Shiba, Neutron scattering study of $Cs_2CoCl_4$: A system of 1D, $S = \frac{1}{2}$ XY antiferromagnetic chains with spin frustration, *J. Magn. Magn. Mater.*, 1983, **31–34**, 1137–1138.

31 W. Fang, H. J. Chen and J. W. Zhang, Theoretical studies of optical spectra and spin-Hamiltonian parameters for $Co^{2+}$ in $Cs_3CoCl_5$ with first-principles calculations and ligand field theory, *Opt. Mater.*, 2025, **158**, 116428.

32 V. A. Komornikov, A. V. Gudymenko, I. S. Timakov and A. A. Kulishov, Phase equilibria, growth, and properties of crystals in the CsCl-$CoCl_2$-$H_2O$ system, *Inorg. Mater. Appl. Res.*, 2023, **14**, 286–292.

33 L. Nataf, F. Aguado, I. Hernández, R. Valiente, J. González, M. N. Sanz-Ortiz, H. Wilhelm, A. P. Jephcoat, F. Baudelet and F. Rodríguez, Volume and pressure dependences of the electronic, vibrational, and crystal structures of $Cs_2CoCl_4$: identification of a pressure -induced piezochromic phase at high pressure, *Phys. Rev. B*, 2017, **95**, 014110.

34 AtH. Trutia and M. Lébl, Optical spectrum of Co(II) in $CsCoCl_3$ single crystals, *Krist. Tech.*, 1969, **4**, 129–133.

35 J. Makovsky, A. Horowitz and D. Gazit, Single crystal growth of $CsCoCl_3$, $Cs_2CoCl_4$, $Cs_3CoCl_5$, $RbCoCl_3$, $Rb_2CoCl_4$, and $Rb_3CoCl_5$, *J. Cryst. Growth*, 1974, **22**, 241–243.

36 H. Soling, G. Johansson, F. Sandberg and T. Norin, The crystal structure and magnetic susceptibility of $CsCoCl_3$, *Acta Chem. Scand.*, 1968, **22**, 2793–2802.

37 J. C. Rivoal, C. Grisolia, J. P. Torre and M. Vala, Magneto-optical evidence of magnon sidebands in $Cs_3CoCl_5$, *J. Phys.*, 1985, **46**, 1709–1716.

38 B. N. Figgis and A. N. Sobolev, $Cs_3CoCl_5$ at 10 K, *Acta Crystallogr., Sect. C:Cryst. Struct. Commun.*, 2001, **57**, 139–140.
39 B. N. Figgis, E. S. Kucharski and P. A. Reynolds, Electron density distribution in $Cs_3CoCl_5$, *Acta Crystallogr., Sect. B: Struct. Sci.*, 1989, **45**, 232–240.
40 L. E. Wenger and T. P. Hanusa, Synthesis without solvent: consequences for mechanochemical reactivity, *Chem. Commun.*, 2023, **59**, 14210–14222.
41 J. D. Loya, S. J. Li, D. K. Unruh and K. M. Hutchins, Mechanochemistry as a tool for crystallizing inaccessible solids from viscous liquid components, *Cryst. Growth Des.*, 2022, **22**, 285–292.
42 F. Cuccu, L. De Luca, F. Delogu, E. Colacino, N. Solin, R. Mocci and A. Porcheddu, Mechanochemistry: new tolos to navigate the uncharted territory of "impossible" reactions, *ChemSusChem*, 2022, **15**, e202200362.
43 K. Kanazawa, S. Yubuchi, C. Hotehama, M. Otoyama, S. Shimono, H. Ishibashi, Y. Kubota, A. Sakuda, A. Hayashi and M. Tatsumisago, Mechanochemical synthesis and characterization of metastable hexagonal $Li_4SnS_4$ solid electrolyte, *Inorg. Chem.*, 2018, **57**, 9925–9930.
44 T. Jardiel, D. G. Calatayud, M. Rodríguez, D. Fernández-Hevia and A. C. Caballero, Synthesis of metastable $Bi_6Ti_5WO_{22}$ phase by the mechanochemical method, *Mater. Lett.*, 2013, **94**, 58–60.
45 T. F. Grigor'eva, S. V. Tsybulya, S. V. Cherepanova, G. N. Kryukova, A. P. Barinova, V. D. Belykh and V. V. Boldyrev, Mechanochemical synthesis of metastable solid solutions: phase composition and microstructure evolution, *Inorg. Mater.*, 2000, **36**, 143–149.
46 E. M. Heppke, A. Koldemir, R. Pöttgen, T. Bredow and M. Lerch, Mechanochemical synthesis and structural evaluation of a metastable polymorph of $Ti_3Sn$, *Z. Naturforsch., B:J. Chem. Sci.*, 2023, **78**, 209–214.
47 Yu. A. Skakov, Formation and stability of metastable phases in mechanochemical synthesis, *Met. Sci. Heat Treat.*, 2005, **47**, 296–304.
48 V. Petříček, L. Palatinus, J. Plášil and M. Dušek, Jana2020 – a new version of the crystallographic computing system Jana, *Z. Kristallogr. - Cryst. Mater.*, 2023, **238**, 271–282.
49 M. Burgelman, P. Nollet and S. Degrave, Modelling polycrystalline semiconductor solar cells, *Thin Solid Films*, 2000, **361–362**, 527–532.
50 M. Burgelman, K. Decock, S. Khelifi and A. Abass, Advanced electrical simulation of thin film solar cells, *Thin Solid Films*, 2013, **535**, 296–301.
51 A. Usman and T. Bovornratanaraks, Modeling nd optimization of modified $TiO_2$ with aluminum and magnesium as ETL in $MAPbI_3$ perovskite solar cells: SCAPS 1D frameworks, *ACS Omega*, 2024, **9**, 39663–39672.
52 M. Fantauzzi, F. Secci, M. Sanna Angotzi, C. Passiu, C. Cannas and A. Rossi, Nanostructured spinel cobalt ferrites: Fe and Co chemical state, cation distribution and size effects by X-ray photoelectron spectroscopy, *RSC Adv.*, 2019, **9**, 19171–19179.
53 M. C. Biesinger, B. P. Payne, A. P. Grosvenor, L. W. M. Lau, A. R. Gerson and R. St. C. Smart, Resolving surface chemical states in XPS analysis of first row transition metals, oxides and hydroxides: Cr, Mn, Fe, Co and Ni, *Appl. Surf. Sci.*, 2011, **257**, 2717–2730.
54 J. Baltrusaitis, B. Mendoza-Sanchez, V. Fernandez, R. Veenstra, N. Dukstiene, A. Roberts and N. Fairley, Generalized molybdenum oxide surface chemical state XPS determination via informed amorphous sample model, *Appl. Surf. Sci.*, 2015, **326**, 151–161.
55 A. Cano, J. Rodríguez-Hernández, L. Reguera, E. Rodríguez-Castellón and E. Reguera, On the scope of XPS as sensor in coordination chemistry of transition metal hexacyanometallates, *Eur. J. Inorg. Chem.*, 2019, **2019**, 1724–1732.
56 W. Breitling, W. Lehmann, T. P. Srinivasan and R. Weber, One phonon Raman scattering of hexagonal $ABX_3$-compounds, *Solid State Commun.*, 1976, **20**, 525–526.
57 W. Breitling, W. Lehmann, T. P. Srinivasan and R. Weber, Raman scattering on the electronic states of $Co^{2+}$ in the 1D Ising antiferromagnet $CsCoCl_3$, *J. Magn. Magn. Mater.*, 1977, **6**, 116–119.
58 O. P. Lamba and S. K. Sinha, Polarized Raman scattering from oriented single crystals of $A_2BX_4$ halides (A = Cs, B = Zn, X = Cl, Br, I), *Solid State Commun.*, 1986, **57**, 365–371.
59 O. P. Lamba, M. B. Patel, S. Ram, P. Chand and H. D. Bist, Raman scattering study of the phase sequence in $A_2BX_4$ halides, *Solid State Commun.*, 1984, **50**, 321–325.
60 B. Briat and J. C. Canit, Polarized absorption and magnetic circular dichroism of the $FeCl_4^{2-}$ ion in a tetragonally distorted tetrahedral site the crystal spectra of $Cs_3FeCl_5$, *Mol. Phys.*, 1983, **48**, 33–61.
61 M. H. Brooker and C.-H. Huang, Raman spectroscopic investigations on the structures of $CsMgCl_3$ and $Cs_3MgCl_5$, *Mater. Res. Bull.*, 1980, **15**, 9–16.
62 M. H. Brooker and J. Wang, Raman studies on the structures and properties of the compounds formed in the $CdCl_2$-CsCl binary system, *J. Raman Spectrosc.*, 1992, **23**, 471–478.
63 H. Seifert, Über die systeme alkalimetallchlorid/Kobalt(II)-chlorid, *Z. Anorg. Allg. Chem.*, 1961, **307**, 137–144.
64 C. F. Putnik and S. L. Holt, 7. Magnon sidebands in the electronic absorption spectra of cesium trichlorocobaltate and rubidium trichlorocobaltate, *Inorg. Chem.*, 1977, **16**, 1010–1016.
65 Y. Xu and M. A. A. Schoonen, The absolute energy positions of conduction and valence bands of selected semiconducting minerals, *Am. Mineral.*, 2000, **85**, 543–556.
66 S. N. S. Nasir, N. A. Mohamed, M. A. Tukimon, M. F. M. Noh, N. A. Arzaee and M. A. M. Teridi, Direct extrapolation techniques on the energy band diagram of $BiVO_4$ thin films, *Physica. B. Condens. Matter.*, 2021, **604**, 412719.
67 R. E. Aderne, B. G. A. L. Borges, H. C. Ávila, F. Von Kieseritzky, J. Hellberg, M. Koehler, M. Cremona, L. S. Roman, C. M. Araujo, M. L. M. Rocco and C. F. N. Marchiori, On the energy gap determination of

organic optoelectronic materials: the case of porphyrin derivatives, *Mater. Adv.*, 2022, **3**, 1791–1803.

68 A. Shafiee and M. Yahaya, Determination of HOMO and LUMO of [6,6]-Phenyl C61-butyric Acid 3-ethylthiophene Ester and Poly (3-octyl-thiophene-2, 5-diyl) through Voltametry Characterization, *Sains Malays.*, 2011, **40**, 173–176.

69 X. Yang, D. Singh and R. Ahuja, Recent advancements and future prospects in ultrathin 2d semiconductor-based photocatalysts for water splitting, *Catalysts*, 2020, **10**, 1–50.

70 F. A. Chowdhury, Recent advances and demonstrated potentials for clean hydrogen via overall solar water splitting, *MRS Adv.*, 2019, **4**, 2771–2785.

71 M. K. Hossain, G. F. I. Toki, A. Kuddus, M. H. K. Rubel, M. M. Hossain, H. Bencherif, M. F. Rahman, M. R. Islam and M. Mushtaq, An extensive study on multiple ETL and HTL layers to design and simulation of high-performance lead-free $CsSnCl_3$-based perovskite solar cells, *Sci. Rep.*, 2023, **13**, 2521.

72 A. Alsalme and H. Alsaeedi, Twenty-two percent efficient Pb-free all-perovskite tandem solar cells using SCAPS-1D, *Nanomaterials*, 2022, **13**, 96.

73 M. Elawad, K. I. John, A. M. Idris, L. Yang and Y. Gao, An organic hole-transporting material spiro-OMeTAD doped with a Mn complex for efficient perovskite solar cells with high conversion efficiency, *RSC Adv.*, 2021, **11**, 32730–32739.